Chapter 8
Broken Rotor Bars in Squirrel Cage Induction Machines – Modeling and Simulation

Christian Kral, Anton Haumer, and Christian Grabner

Abstract This paper presents a physical model of a squirrel cage induction machine with rotor topology. The machine is modeled in Modelica, an object oriented multi physical modeling system. The presented machine model is used to investigate electrical rotor asymmetries in induction machines. For the case of a single broken rotor bar a simulation model is compared with measurement results.

Keywords Modelica · induction machines · squirrel cage · rotor asymmetries · broken rotor bar

8.1 Introduction

The squirrel cage of an induction machine can be seen as a multiphase winding with shorted turns. Instead of a wound structure the rotor consists of N_r bars and two end rings, connecting the bars on both ends, as depicted in Fig. 8.1. At the end rings fins are located to force the circulation of air in the inner region of the machine.

In the production plant it is intended to fabricate a fully symmetrical squirrel cage. Yet, manufacturing tolerances and technological uncertainties give rise to inhomogeneous material densities. These inhomogeneities cause unequal rotor bar and end ring resistances – the so called electrical rotor asymmetries. The causes for such rotor electrical asymmetries are:

- Shrink holes and voids in the material of the bars or end rings
- Improper junctions of the bars and end rings
- Heavy duty start-ups that the machine is not designed for
- Thermal overloading of the machine
- High temperature gradients, causing cracks

C. Kral (✉), A. Haumer, and C. Grabner
Electric Drive Technologies, Austrian Institute of Technology,
Giefinggasse 2, 1210 Vienna, Austria
e-mail: christian.kral@ait.ac.at; anton.haumer@ait.ac.at;
christian.grabner@ait.ac.at

S.-I. Ao and L. Gelman (eds.), *Electronic Engineering and Computing Technology*,
Lecture Notes in Electrical Engineering 60, DOI 10.1007/978-90-481-8776-8_8,

Fig. 8.1 Scheme of a rotor cage of an induction machine

The presented machine topology is modeled in *Modelica*, an acausal object oriented modeling language for multi physical systems [3]. In the *Modelica Standard Library* (MSL) a standard set of physical packages for electric, mechanic, thermal, control and logic components is collected. The *Machines* package provides models of electric machines based on text book equations. The modeled three phase induction machines rely on space phasor theory and a full symmetry of the stator and rotor winding. Electrical rotor asymmetries can therefore not be modeled using the MSL.

In order to model electrical rotor asymmetries the full topology of the rotor cage, respectively has to be taken into account. Such models are developed in the *ExtendedMachines* Library [5].

8.2 Model of Stator Winding

It is assumed in the following that the stator winding is fully symmetrical. Additionally, the number of stator phases is restricted to three. In this case the stator voltage equation can be written as

$$V_{s[i]} = R_s I_{s[i]} + L_{s\sigma}\frac{\mathrm{d}I_{s[i]}}{\mathrm{d}t} + \sum_{j=1}^{3} L_{sm[i,j]}\frac{\mathrm{d}I_{s[j]}}{\mathrm{d}t} + \sum_{j=1}^{N_r}\frac{\mathrm{d}L_{sr[i,j]}I_{r[j]}}{\mathrm{d}t}, \tag{8.1}$$

where $V_{s[i]}$ and $I_{s[i]}$ and $I_{r[i]}$ are the stator voltages and stator currents and the rotor currents, respectively. The stator resistance R_s and the stator stray inductance $L_{s\sigma}$ are symmetrical, due to the symmetry of the stator winding. The coupling of the stator windings is represented by the main field inductance matrix

$$L_{sm[i,j]} = L_0 w_s^2 \xi_s^2 \cos\left[\frac{(i-j)2\pi}{3}\right]. \tag{8.2}$$

The mutual coupling between the stator and rotor is represented by the matrix

$$L_{sr[i,j]} = L_0 w \xi_s \xi_r \cos\left[\frac{(i-1)2\pi}{3} - \frac{(j-1)2\pi}{N_r} - \gamma_m\right]. \tag{8.3}$$

Both these matrices are fully symmetrical, since it is assumed that the coupling over the magnetic main field is not influenced by the any electric asymmetry. The term L_0 indicates the base inductance of a coil without chording, i.e., the coil width equal to the pole pitch. The number of series connected turns and the winding factor of the stator winding are represented by the parameters w_s and ξ_s. The product $w_s\xi_s$ is thus the *effective number of turns.* The winding factor of the rotor winding

$$\xi_r = \sin\left(\frac{p\pi}{N_r}\right) \tag{8.4}$$

is a pure geometric factor, which is derived from the mesh width of two adjacent rotor bars. In this equation, however, skewing is not considered. The quantity γ_m represents the electric displacement angle of the rotor with respect to the stator.

The effective number of turns, $w_s\xi_s$, can be determined from a winding topology, which is indicated by the begin and end location and the number of turns of the stator winding coils. Alternatively, a symmetric stator winding may be parametrized by entering the effective number of turns.

8.3 Model of Rotor Winding

The winding topology of the squirrel cage rotor with N_r rotor bars can be seen as a winding with an effective number of turns equal to one. The matrix of the main rotor field can be expressed as

$$L_{rr[i,j]} = L_0 \xi_r^2 \cos\left[\frac{(i-j)2\pi}{N_r}\right]. \tag{8.5}$$

For the bars and the end rings on both sides (index a = drive end side, DE; index b = non drive end, NDE) constant leakage inductances $L_{b[i]}$ and $L_{ea[i]}$ and $L_{eb[i]}$ are considered. The rotor voltage equations can be derived from the equivalent circuit of a rotor mesh as shown in Fig. 8.2:

$$\begin{aligned}
0 = {} & (R_{ea[i]} + R_{eb[i]} + R_{b[i]} + R_{b[i+1]})I_{r[i]} - R_{b[i]}I_{r[i-1]} - R_{b[i+1]}I_{r[i]} \\
& + R_{eb[i]}I_{eb} + (L_{ea[i]} + L_{eb[i]} + L_{b[i]} + L_{b[i+1]})\frac{dI_{r[i]}}{dt} \\
& - \frac{d}{dt}(L_{b[i]}I_{r[i-1]} + L_{b[i+1]}I_{r[i]} - L_{eb[i]}I_{eb}) \\
& + \sum_{j=1}^{3} \frac{dL_{sr[j,i]}I_{s[j]}}{dt} + \sum L_{rr[i,j]}\frac{dI_{r[j]}}{dt}
\end{aligned} \tag{8.6}$$

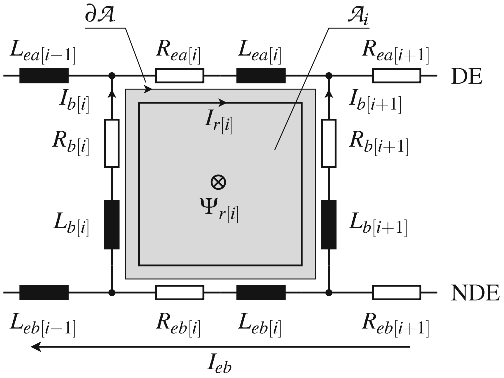

Fig. 8.2 Rotor cage topology (DE = drive end, NDE = non drive end)

In this equation $R_{b[i]}$ are the bar resistances, and $R_{ea[i]}$ and $R_{eb[i]}$ are the resistances of the end ring segments on both sides. Due to the topology of the rotor cage (Fig. 8.2), $N_r + 1$ linearly independent meshes have to be taken into account. The mesh current I_{eb} is thus introduced and the additional voltage equation

$$0 = \sum_{i=1}^{N_r} R_{eb[i]}(I_{r[i]} + I_{eb}) + \frac{\mathrm{d}}{\mathrm{d}t} \sum_{i=1}^{N_r} L_{eb[i]}(I_{r[i]} + I_{eb}) \tag{8.7}$$

has to be considered, accordingly.

As the air gap of the induction machine is modeled with smooth surface, the main field inductances $L_{ss[i,j]}$ and $L_{rr[i,j]}$ are constant and only the mutual inductances (8.3) are a function of the rotor angle γ_m.

The rotor cage can be parametrized in the *ExtendedMachines* library in two different ways. First, a symmetric rotor cage can be indicated by the rotor resistance R_r' and the rotor leakage inductance $L_{r\sigma}'$, equivalently transformed to the stator side. These are the typical parameters as they appear in the an equivalent circuit of the induction machine. The same parameters are also used for the Machines package of the MSL. Second, each resistance and leakage inductance of the rotor bars and the end ring segments on both sides can be parametrized. The relationship between the symmetric rotor bar and end ring resistance and the rotor resistance with respect to the stator side is determined by

$$R_r' = 2\frac{3w_s^2\xi_s^2}{N_r\xi_r^2}\left\{R_{e,\mathrm{sym}} + R_{b,\mathrm{sym}}\left[1 - \cos\left(\frac{2\pi p}{N_r}\right)\right]\right\}, \tag{8.8}$$

where p is the number of pole pairs. A similar equation can be obtained for the rotor leakage inductance with respect to the stator side,

$$L_{r\sigma}' = 2\frac{3w_s^2\xi_s^2}{N_r\xi_r^2}\left\{L_{e\sigma,\mathrm{sym}} + L_{b\sigma,\mathrm{sym}}\left[1 - \cos\left(\frac{2\pi p}{N_r}\right)\right]\right\}. \tag{8.9}$$

For the symmetric cage the ratios of the resistances, ρ_r, and leakage inductances, ρ_l, each with respect to the rotor bars over the end ring segments, can be specified,

$$\rho_r = \frac{R_{b,\mathrm{sym}}}{R_{e,\mathrm{sym}}}, \tag{8.10}$$

$$\rho_l = \frac{L_{b\sigma,\mathrm{sym}}}{L_{e\sigma,\mathrm{sym}}}. \tag{8.11}$$

This way, the symmetric cage resistance and leakage inductance parameters can be determined from R'_r, $L'_{r\sigma}$, ρ_r and ρ_l.

An electric rotor asymmetry can be modeled by increasing the resistance of a rotor bar or and end ring segment, respectively. Alternatively the equation structure could be adopted by removing a completely broken bar or end ring segment accordingly – this case is, however, not considered in this paper.

8.4 Torque Equation

The inner electromagnetic torque of the machine is determined by

$$T_{\mathrm{el}} = \sum_{i=1}^{3} \sum_{j=1}^{N_r} \frac{\mathrm{d}L_{sr[i,j]}}{\mathrm{d}\gamma_m} I_{s[i]} I_{r[j]}, \tag{8.12}$$

where $\frac{\mathrm{d}L_{sr[i,j]}}{\mathrm{d}\gamma_m}$ can be expressed analytically from (8.3). Even if friction, ventilation losses and stray load losses are not taken into account in the presented paper, they could be considered as a breaking torque in the angular momentum equation.

8.5 Theoretical Background of Rotor Faults

An electrical rotor asymmetry gives rise to a distortion of the rotor bar currents and the fundamental wave of the rotor magneto motive force (MMF). Therefore, the fundamental rotor MMF can be decomposed into a forward and backward traveling wave with respect to the rotor fixed reference frame. The forward travelling wave represents the main magnetic field and the backward traveling wave is due to the electrical rotor asymmetry. For infinite inertia drives the backward travelling wave induces a stator voltage harmonic component at the frequency

$$f_l = (1 - 2s) f_s. \tag{8.13}$$

In this equation f_s is the stator supply frequency and

$$s = \frac{f_s - pn}{f_s} \tag{8.14}$$

is slip, expressed in terms of rotor speed n and the number of pole pairs. The impedance of the machine (including supply) leads to a stator current harmonic with the same frequency as the induced stator voltage harmonic. Since the frequency of this harmonic component is less than the frequency of the fundamental wave this stator current harmonic component is called the *lower side band* harmonic. A finite inertia of the drive causes an additional upper side band harmonic current at frequency

$$f_u = (1 + 2s) f_s, \tag{8.15}$$

the *upper side band harmonic* [2]. Due to the interaction of these side band currents with flux and the inertia specific speed ripple, additional harmonics arise,

$$f_{l[k]} = (1 - 2ks) f_s, \tag{8.16}$$

$$f_{u[k]} = (1 + 2ks) f_s, \tag{8.17}$$

where k is an integer order number. Between no load and rated operating conditions slip varies between zero and some per cent.

The side band currents of stator currents are also reflected in the flux linkages of the main field (air gap) [9] and the stray flux [4]. The interaction of the fundamental and harmonic waves of the currents and flux linkages gives rise to double slip frequency oscillations

$$f_t = 2sf_s \tag{8.18}$$

of the electrical power and torque. The magnitudes of these fault specific oscillations are much smaller the average values of the electrical power and torque, respectively.

8.6 Investigated Machine

The investigated simulation and measurement results refer to a 18.5 kW, four pole induction machine with 40 rotor bars (Fig. 8.3). The experiments were performed for nominal load torque, nominal line-to-line voltage (400 V) and nominal frequency (50 Hz). For experimentally investigating electric asymmetries one rotor bar was fully broken by drilling a hole into the aluminum part of the rotor as shown in Fig. 8.3b.

For the investigated machine and design geometry the parameters of the rotor bar and end ring segments, $R_{b,\mathrm{sym}}$, $L_{b\sigma,\mathrm{sym}}$, $R_{e,\mathrm{sym}}$ and $L_{e\sigma,\mathrm{sym}}$ are estimated according to (8.8)–(8.11) for a given rotor resistance R_r' and a leakage inductance $L_{r\sigma}'$. In the

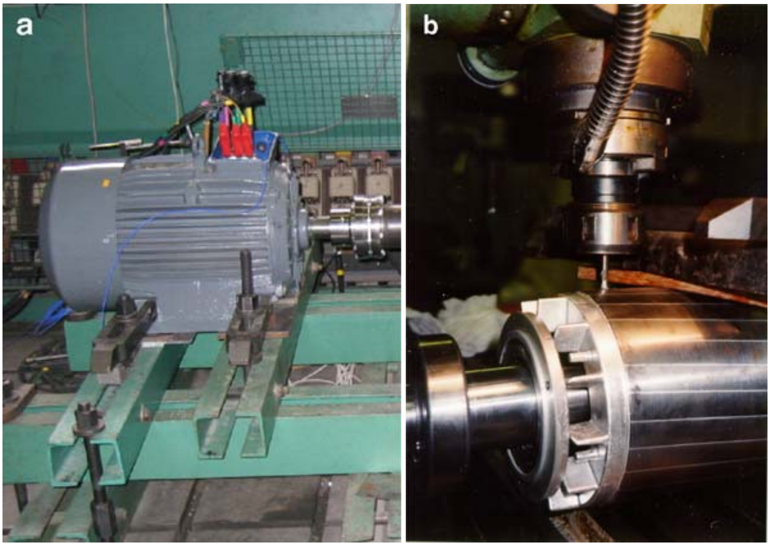

Fig. 8.3 (**a**) 18.5 kW four pole induction machine in the lab, (**b**) drilling a hole into the aluminum part of the squirrel cage rotor

simulation the broken bar was modeled by setting the faulty bar resistance with index 1 to

$$R_{b[1]} = 100 R_{b,\mathrm{sym}}. \tag{8.19}$$

This is enough resistance increase for the respective bar current to sufficiently vanish.

8.7 Simulation Results

The distortion of the current distribution of the rotor bars and end ring segments due to an electrical rotor asymmetry is evident. The rotor bar currents can be computed from the rotor mesh currents according to Fig. 8.2,

$$I_{b[i]} = I_{r[i]} - I_{r[i-1]}. \tag{8.20}$$

Under nominal and steady state operating conditions the peak values of the sinusoidal currents of the rotor bars are depicted in Fig. 8.4. The current of the broken rotor bar (index 1) is almost zero. Additionally, an interesting phenomenon can be observed. The currents of the adjacently located rotor bars (e.g. index 40 and 2) are significantly larger than the currents of the remaining healthy rotor bars. Due to increased currents in the adjacent rotor bars the associated heat losses increase. If the adjacent bars fail as a result of the increased thermal stress, the extent of the

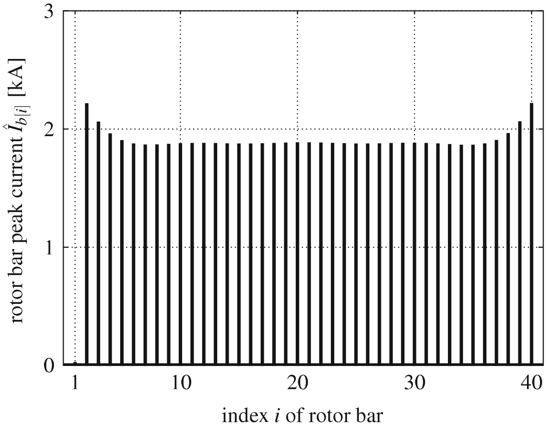

Fig. 8.4 Peak values of the rotor bar currents; broken rotor bar with index 1; simulation results

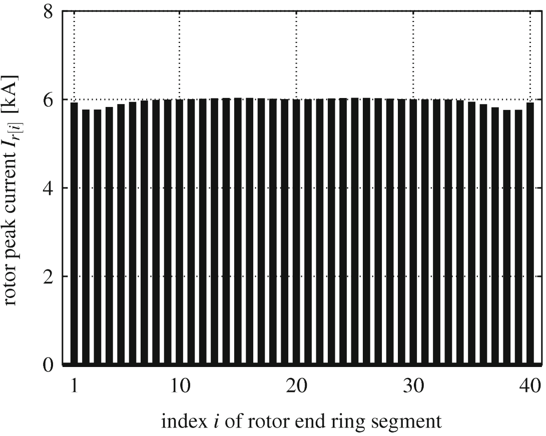

Fig. 8.5 Peak values of the currents of the end ring segments; broken rotor bar with index 1; simulation results

fault may spread in an avalanche-like way. Electrical rotor asymmetries spread relatively slow compared to other machine faults. It will thus take weeks, months or even years for a rotor failure to significantly increase.

Caused by the distortion of the current distribution in the rotor bars, the end ring current are distorted, too. Mathematically, the rotor end ring currents of the A- and B-side can be expressed by

$$I_{ea[i]} = I_{r[i]}, \tag{8.21}$$

$$I_{eb[i]} = I_{r[i]} + I_{eb}. \tag{8.22}$$

Without any asymmetry on either side of the end rings, the mesh current $I_{eb} = 0$ and thus the currents of the end ring segments of the A- and B-side are equal. The peak values of the currents of the rotor end ring segments are depicted in Fig. 8.5 for the case of one broken rotor bar.

The rotor asymmetry specific lower and upper side band harmonics of the current arise close to the fundamental wave according to (8.13) and (8.15). For the investigated 50 Hz machine the Fourier spectrum of a stator current (phase 1) is depicted in Fig. 8.6. The lower and upper side band harmonics clearly appear at 48.6 Hz and 51.4 Hz. Since the magnitudes of these side band components are much smaller than the magnitude of the fundamental, electrical rotor asymmetries are difficult to detect.

8.8 Measurement Results

In Fig. 8.7 the measured Fourier spectrum of a stator phase current is depicted. This plot reveals compared to the simulation results of Fig. 8.6 the same frequencies of the side band harmonics, but slightly deviating magnitudes. The differences of the magnitudes are mainly due to the inertia of the drive which is not exactly estimated [7]. Some additional deviation of the modeled rotor bar and end ring resistance ratio

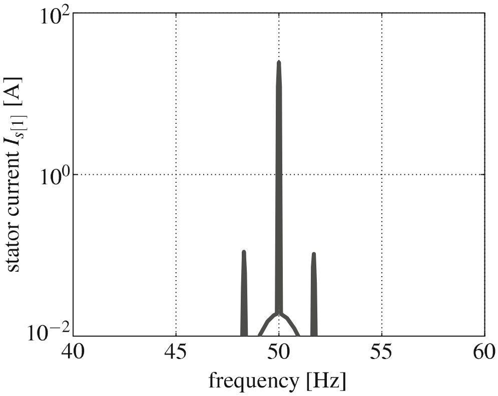

Fig. 8.6 Fourier spectrum of the stator current $I_{s[1]}$; simulation results

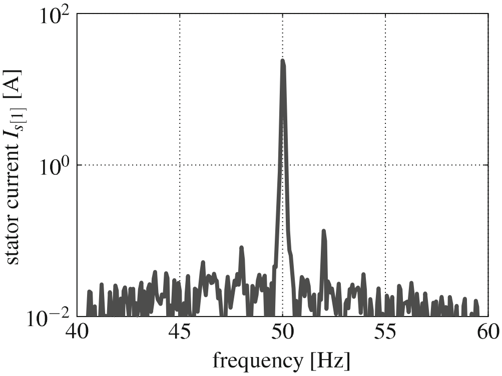

Fig. 8.7 Fourier spectrum of the stator current $I_{s[1]}$; measurement results

from the real machine cage, also have an impact on the magnitudes of the side band currents. With respect to the comparison of measurement and simulation results it should also be noted that in a real motor with die-cast rotor interbar currents arise [10].

8.9 Rotor Fault Detection Methods

Since the magnitudes of the fault specific current harmonics are much smaller than the fundamental wave current, only severe rotor asymmetries can be detected through visual observations of fluctuations of the current or power pointer instruments. For the detection of upcoming electric rotor asymmetries require some more sophisticated detection methods have to be used. The most common rotor fault detection methods are based on the measurement of one stator current – this class of methods is called *current signature analysis* (CSA) methods [1]. Then a fast Fourier transform or a wavelet transform or some other signal processing techniques are performed in order to determine the fault specific current harmonic side bands.

Another class of methods uses *power signature analysis* (PSA), evaluating either total or phase power [8]. For the assessment of the fault severity – in combination with either CSA or PSA techniques – neural networks or Fuzzy based methods may be applied.

A third class of fault detection methods uses model based techniques for the detection of rotor faults. One model based technique is the Vienna Monitoring Method (VMM) which was introduced in 1997 [11]. The VMM compares the calculated torques of a voltage and a current model to derive a fault indicator. If the models are well tuned, both models compute the same torque in case of a fully symmetrical rotor cage. An electrical rotor asymmetry excites double slip frequency torque oscillations in both models – with different magnitude and phase shift, however. The magnitude of the derived torque difference is directly proportional to the average load torque. This relationship can be used to calculate a robust fault indicator. For this purpose the torque difference is divided by the estimated load torque which leads a new quantity: the relative torque difference. A spacial data clustering technique, applied to the relative torque difference, then eliminates any harmonic components which is not an integer multiple of slip frequency. The magnitude of second harmonic of the relative torque difference can the be determined by applying a discrete Fourier analysis of the clustered data values, and serves as fault indicator for the VMM. The particular advantage this technique is that it provides a reliable fault indicator independent of load torque, speed, supply and inertia of the drive [6, 7].

The VMM is applied to both the simulation and measurement results. The fault indicator determined from the simulation and measurement results is 0.0093 and 0.0105, respectively. The deviation of these two quantities is about 11%.

8.10 Conclusions

For induction machines with squirrel cage rotors the background of electrical rotor asymmetries is introduced and discussed. A rotor topology model as it is implemented in the *ExtendedMachines*, is presented.

For a 18.5 kW induction machine with one broken rotor bar – out of 40 bars – simulated and measured results are compared and shown good coherence. The results refer to the Fourier spectra of the stator currents and a model based rotor fault detection method – the Vienna Monitoring Method. The comparison of the fault indicators determined by the Vienna Monitoring Method for the simulation and measurement case, reveals a deviation of about 11%. Considering that no parameter tuning of the simulation model has been performed, this is a satisfactory matching result.

References

1. Didier, G., Ternisien, E., Caspary, O., Razik, H.: Fault detection of broken rotor bars in induction motor using a global fault index. IEEE Trans. Ind. Appl. **42**(1), 79–88 (2006)
2. Filippetti, F., Franceschini, G., Tassoni, C., Vas, P.: Impact of speed riple on rotor fault diagnosis of induction machines. Proceedings of the International Conference on Electrical Machines, ICEM, pp. 452–457, 1996
3. Fritzson, P.: Principles of Object-Oriented Modeling and Simulation with Modelica 2.1. IEEE Press, Piscataway, NJ, 2004
4. Henao, H., Demian, C., Capolino, G.-A.: A frequency-domain detection of stator winding faults in induction machines using an external flux sensor. IEEE Trans. Ind. Appl. **39**, 1272–1279 (2003)
5. Kral, C., Haumer, A., Pirker, F.: A modelica library for the simulation of electrical asymmetries in multiphase machines – the extended machines library. IEEE International Symposium on Diagnostics for Electric Machines, Power Electronics and Drives, The 6th, SDEMPED 2007, Cracow, Poland, pp. 255–260, 2007
6. Kral, C., Pirker, F., Pascoli, G.: Model-based detection of rotor faults without rotor position sensor – the sensorless vienna monitoring method. IEEE Trans. Ind. Appl. **41**(3), 784–789 (2005)
7. Kral, C., Pirker, F., Pascoli, G.: The impact of inertia on rotor fault effects – theoretical aspects of the vienna monitoring method. IEEE Trans. Power Electron. **23**(4), 2136–2142 (2008)
8. Liu, Z., Yin, X., Zhang, Z., Chen, D., Chen, W.: Online rotor mixed fault diagnosis way based on spectrum analysis of instantaneous power in squirrel cage induction motors. IEEE Trans. Energy Conver. **19**(3), 485–490 (2004)
9. Schagginger, M.: Luftspaltfelduntersuchungen an umrichtergespeisten Asynchronmaschinen im Hinblick auf elektrische Unsymmetrien im Rotorkäfig. Master's thesis, Technische Universität Wien, Vienna, 1997
10. Walliser, R.: The influence of interbar currents on the detection of broken rotor bars. ICEM, pp. 1246–1250, 1992
11. Wieser, R., Kral, C., Pirker, F., Schagginger, M.: On-line rotor cage monitoring of inverter fed induction machines, experimental results. Conference Proceedings of the First International IEEE Symposium on Diagnostics of Electrical Machines, Power Electronics and Drives, SDEMPED, pp. 15–22, 1997